

Article

An Integrated Software for Computing Mechanical Properties of Crystalline Material by Means of XRD

Vinh Phoi Nguyen ¹, Anh Van Ha Nguyen ², Chi Cuong Le ³ and Thien Ngon Dang ^{3,*}

¹ Faculty of Engineering and Technology, Pham Van Dong University, Quang Ngai 570000, Vietnam; nvphoi@pdu.edu.vn

² Faculty of Engineering Maritime College No.2, Ho Chi Minh 700000, Vietnam; nguyenanhvanha@cdhanghai.edu.vn

³ Faculty of Mechanical Engineering, HCMC University of Technology and Education, Ho Chi Minh 700000, Vietnam; lccuong@hcmute.edu.vn

* Correspondence: ngondt@hcmute.edu.vn; Tel.: +84-91-3804-3803

Abstract: An integrated software for calculating the major mechanical properties of materials was newly programmed. The material mechanical properties are determined from a peak position and the broadness of X-ray diffraction (XRD) line using profile function method, including Gaussian, Parabola, Half-width, and Centroid. The X-ray diffraction line in software is also corrected by the generalized X-ray absorption function. The results show that the precision coefficient (R^2) of the $d_{hkl}\text{-sin}^2\psi$ linear regression depends on tested materials and the method of the 2θ determination. The Parabola and Gaussian methods show greater fitting accuracy in comparison to the other two methods in determining stress. The mechanical properties calculated using this software agreed well with the values determined from the conventional methods. In addition, this XRD software also allows computing the 95% confidential limits of the results from a single measurement without conducting repetitive measurements. Therefore, the new software allows widening the experimental scopes of an X-ray diffraction device in both laboratories and the industrial sector.

Keywords: X-ray diffraction; hardness evaluation; residual stress; analysis of phase compositions; integrated software



Citation: Nguyen, V.P.; Nguyen, A.V.H.; Le, C.C.; Dang, T.N. An Integrated Software for Computing Mechanical Properties of Crystalline Material by Means of XRD. *Appl. Sci.* **2021**, *11*, 9523. <https://doi.org/10.3390/app11209523>

Academic Editor: Roberto Zivieri

Received: 16 August 2021

Accepted: 4 October 2021

Published: 13 October 2021

Publisher's Note: MDPI stays neutral with regard to jurisdictional claims in published maps and institutional affiliations.



Copyright: © 2021 by the authors. Licensee MDPI, Basel, Switzerland. This article is an open access article distributed under the terms and conditions of the Creative Commons Attribution (CC BY) license (<https://creativecommons.org/licenses/by/4.0/>).

1. Introduction

Since they were discovered in 1890, X-rays and the techniques using X-ray diffraction [1,2] have shown great progress and have seen a variety of applications in industry because of their advantages over other nondestructive techniques. They can evaluate many mechanical properties including stress [2–4], crystalline grain size [5], phase composition analysis [6,7], hardness [8], the thickness of plating or coating layer [9,10], etc. Moreover, X-ray diffraction has also been used to identify modifications of phase, texture, dislocation density, and mechanical twins of materials [11]. Ultrasonic and magnetic techniques have many applications for many kinds of materials at the macro level to determine material inhomogeneity; however, they cannot determine the properties at the micro- and nano-level. The laser technique can only determine the outer profile of the sample surface such as roughness. The microscopic technique is used to observe crystalline microstructure, and when combined with image processing, it can determine crystal grain size, phase components in multi-phase materials, and layer thickness [12]; however, it has difficulty in determining the state of materials such as stress, hardness, etc. Fortunately, X-rays with short wavelengths can detect the change or characteristics of a crystalline matrix from macro- to micro- and even nano-level, and it can therefore determine the hereabove parameters of crystalline materials. Moreover, a distinguished advantage of the XRD method over the other methods is that it can determine the standard deviations from a single measurement without replication of measurement. This is because the diffraction of

photons in the crystal matrix occurs in all directions, and thus functions calculated from X-ray counting, such as peak position, stress, line width, and others, are random functions and contain coherent reproducibility of measured values [13,14].

On the other hand, in order to obtain the correct value of X-ray intensity, and thus the accurate peak position and the full width at half of the diffraction line, the diffracted X-ray intensity must be corrected for the Lorentz-polarization and absorption factor [2,15,16]. The absorption factor for only the iso-inclination method (Ω -type goniometer) using the fixed- ψ method was computed and widely used [16]. However, the position-sensitive proportional counter (PSPC), in which the incident beams are fixed during the scanning process (fixed- ψ_0 method), is used more widely. Moreover, to increase the diffraction angle 2θ up to approximately 170° and the inclination angle ψ up to approximately 165° , the side-inclination method (Ψ -type goniometer) is used. For these measurement methods, the absorption factor is still not fully derived and is not embedded in commercial X-ray systems. Furthermore, there are many methods of approximating the diffraction line to determine the diffraction peak. The choice of mathematical function to interpolate the peak diffraction greatly affected the accuracy of the measurement results. This has been reported in stress measurements using X-ray diffraction (XRD) [17,18]. To enlarge the scope of application of XRD for various measurements in a single device, there should be a computation system that can accurately determine many material properties. In a previous study, automated controlling and calculating software using C++ and commercial MS Excel was used for determining the residual stress of polycrystalline materials [13]. This research represents a new computation program for polycrystalline materials that determines their properties using XRD, with total integration of absorption factors and mathematical function for the correction of diffraction lines. It can evaluate common mechanical properties in industry. The following measurements are carried out:

- i. Residual stress computation for the aluminum alloy A1060;
- ii. Surface hardness of quenched and tempered carbon steel JIS-type S50C;
- iii. Quantitative analysis for triple-phase carbide T15K6 containing three phases, WC, TiC, and Co;
- iv. Thickness measurement of the nickel-coating layer on substrate carbon steel S45C;
- v. Determining grain size of the zeolite material ZSM-5.

The demonstration measurements using X-rays and conventional methods were also compared to verify the validity of the computation and thus the applicability to the manufacturing site. All XRD measurements in this study use the X-ray characteristic $\text{CuK}\alpha$ with a wavelength λ of 1.5 \AA and Ni foil filter. The use of a graphical user interface (GUI) also allows beginner-level programmers to easily reprogram resource codes for their individual computation.

2. Material Analyzing Software

2.1. Selection of Development Language

Structured programming (SP) languages such as Basic, Pascal, and C have a common structure [19]:

$$\text{Programs} = \text{Data structures} + \text{Algorithms}$$

The advantage of SP includes ease of following; however, for large projects, the resource code cannot be reused and the algorithm strictly depends on the data structure. In contrast, object-oriented programming languages, including Turbo Pascal, C++, and C#, use the classes containing functions and variables to solve tasks of the objects [20]. Among these strong languages, C# is a .NET Framework background language, and is easy for programmers to use since it has various libraries of functions and parameters [20,21]. Therefore, in this study, C# is used to build the new analyzing software XPro 2.0.

The routine of the software is as below:

Step 1: Measurement data are read. They are raw data files, obtained from the commercial X-ray diffractometer, which is Panalytical XPert system in this paper.

- Step 2: Analyzing X-ray diffraction lines; background and LPA factor correction.
- Step 3: Determining peak positions with many mathematical functions.
- Step 4: Calculation of the mechanical properties.
- Step 5: Representation of computed values.

2.2. Lorentz-Polarization and Absorption (LPA) Factor

There are two inclination methods using X-ray diffraction, including the iso- and side-inclination methods (sometimes called Ω - and Ψ -type goniometers); however, the latter gives measurement at higher ψ angles. The absorption function for iso-inclination has been calculated [16]; however, side-inclination has not been calculated. Therefore, this research will introduce the determination of the general absorption function for material using the iso- and side-inclination method.

Figures 1 and 2 show the incident beam AO and diffracted beam OB from a material fraction with sizes $l_1 \times l_2 \times dz$ at the depth z from the surface. OD is the diffraction plane normal. The incident and diffraction beams, respectively, make angles α and β to the normal of the specimen. 2θ is the diffraction angle and $\eta = 90^\circ - \theta$. The angles ψ_0 and ψ are the angles between incident beam and normal of the diffraction plane. Therefore, the X-ray intensity diffracted from the fraction is given by

$$dI = aI_0 \exp[-\mu(AB + BC)]Sdz \tag{1}$$

where a is the diffraction efficiency and μ is the linear absorption coefficient of the measured material. The irradiated area S is rectangular with the dimensions l_1 and l_2 . AB and BC in Equation (1) are $AB = \frac{z}{\cos \alpha}$, $BC = \frac{z}{\cos \beta}$

$$I = \int_0^\infty I_0 a \exp\left[-\mu\left(\frac{z}{\cos \alpha} + \frac{z}{\cos \beta}\right)\right] l_1 l_2 dz$$

$$\Rightarrow I = \frac{I_0 a}{\mu} l_1 l_2 \frac{\cos \alpha \cdot \cos \beta}{\cos \alpha + \cos \beta}$$

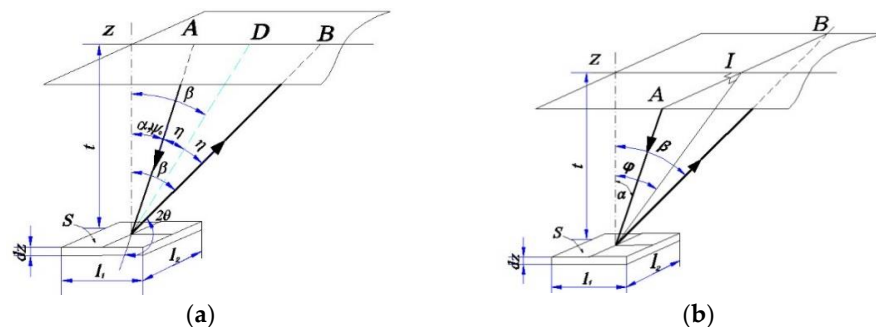


Figure 1. X-ray diffraction methods. (a) Iso-inclination method; (b) Side-inclination method.

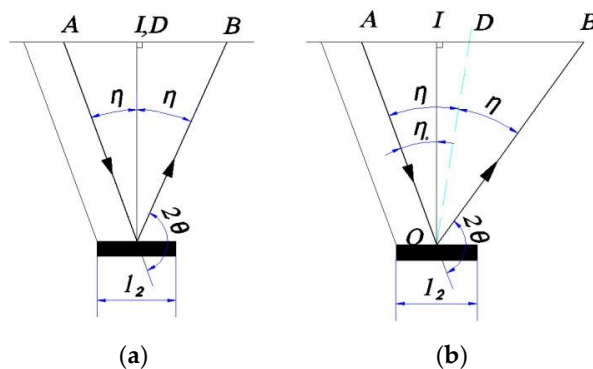


Figure 2. Path length in the side-inclination method. (a) Fixed- η method; (b) Fixed- η_0 method.

Omitting the constants, we obtain the generalized absorption factor for anisotropic material:

$$A = \frac{I}{I_0} = l_1 l_2 \frac{\cos \alpha \cdot \cos \beta}{\cos \alpha + \cos \beta} \quad (2)$$

2.2.1. Without Limitation of the Irradiated Area

In the case of the Iso-inclination method without limitation of the irradiated area, substituting $l_1 = 1/\cos \alpha$ and $l_2 = 1$ into Equation (2) gives us:

$$A = \frac{1}{\cos \alpha} \frac{\cos \alpha \cos \beta}{\cos \beta + \cos \alpha} \quad (3)$$

In the fixed- ψ_0 method, the following relations hold: $\alpha = \psi_0$, $\beta = \psi_0 + 2\eta$, $\eta = 90^\circ - \theta$. Substituting these Equations into the generalized Equation (3), we have the absorption factor for the fixed- ψ_0 method:

$$A = \frac{-\cos(\psi_0 - 2\theta)}{\cos \psi_0 - \cos(\psi_0 - 2\theta)} \quad (4)$$

In the fixed- ψ method, the following relation holds:

$$\begin{cases} \cos \alpha = \sin(\psi + \theta) \\ \cos \beta = \cos(\psi + 90^\circ - \theta) = -\sin(\psi - \theta) \end{cases}$$

By substituting the relation into the generalized absorption factor in Equation (3), we obtain the absorption factor in the fixed- ψ method:

$$A = \frac{-\sin(\psi - \theta)}{\sin(\psi + \theta) - \sin(\psi - \theta)} = 1 - \tan \psi \cot \theta \quad (5)$$

In the case of the side-inclination method, by substituting $l_1 = 1/\cos \psi$ and $l_2 = 1/\cos \eta$ into Equation (2), we obtain the generalized absorption factor:

$$A = \frac{1}{\cos \psi \cos \eta} \frac{\cos \alpha \cos \beta}{\cos \alpha + \cos \beta} \quad (6)$$

In the fixed- η_0 method, the incident x-rays make an angle η_0 to the normal specimen, and we have $\cos \alpha = \cos \psi \sin \eta_0$ and $\cos \beta = \cos \psi \sin \eta^*$ where $\eta^* = 180^\circ - 2\theta - \eta_0$ and $\eta_0 = 90^\circ - \theta_0$. Substituting the above relations into Equation (6), we have the absorption function:

$$A = \frac{\sin(2\theta - \theta_0)}{\sin \theta_0 + \sin(2\theta - \theta_0)} \quad (7)$$

In the fixed- η method, by substituting $\theta_0 = \theta$ into Equation (7), we obtain the absorption function:

$$A = \frac{1}{2} \quad (8)$$

Since A is a constant, the absorption correction in this method is omitted.

2.2.2. With Limitation of the Irradiated Area

In the case of the Iso-inclination method without limitation of the irradiated area, substituting $l_1 = 1$ and $l_2 = 1$ into Equation (2) gives us:

$$A = \frac{\cos \alpha \cos \beta}{\cos \beta + \cos \alpha} \quad (9)$$

In the fixed- ψ_0 method, the following relations hold: $\alpha = \psi_0$, $\beta = \psi_0 + 2\eta$, $\eta = 90^\circ - \theta$. Substituting these Equations into the generalized Equation (9) gives us the absorption factor for the fixed- ψ_0 method:

$$A = \frac{-\cos \psi_0 \cdot \cos(\psi_0 - 2\theta)}{\cos \psi_0 - \cos(\psi_0 - 2\theta)} \tag{10}$$

In the fixed- ψ method, the following relation holds:

$$\begin{cases} \cos \alpha = \sin(\psi + \theta) \\ \cos \beta = \cos(\psi + 90^\circ - \theta) = -\sin(\psi - \theta) \end{cases}$$

Substituting the relation into the generalized absorption factor in Equation (9), we obtain the absorption factor in the fixed- ψ method:

$$A = \frac{\cos 2\psi - \cos 2\theta}{4 \cdot \sin \theta \cdot \cos \psi} \tag{11}$$

In the case of the side-inclination using the fixed- η_0 method, the incident X-rays make an angle η_0 to the normal specimen, and we have $\cos \alpha = \cos \psi \sin \eta_0$ and $\cos \beta = \cos \psi \sin \eta^*$ where $\eta_0 = 90^\circ - \theta_0$ and $\eta^* = 180^\circ - 2\theta - \eta_0$. Substituting the above relations into Equation (9), we have the following absorption function:

$$A = \frac{\cos \psi \cdot \sin \theta_0 \cdot \sin(2\theta - \theta_0)}{\sin \theta_0 + \sin(2\theta - \theta_0)} \tag{12}$$

In the fixed- η method, substituting $\theta_0 = \theta$ into Equation (12), we obtain the absorption function:

$$A = \frac{1}{2} \cos \psi \cdot \sin \theta \tag{13}$$

2.3. Analysis of Diffraction Line

Figure 3 shows the X-ray intensities obtained from the measurement data files measured from the diffraction device. The most important line parameters include line peak position p and broadness B for specific diffraction planes (hkl), which are computed and displayed on the screen. The peak position determination methods and correction for the LPA factor and the background can be selected.

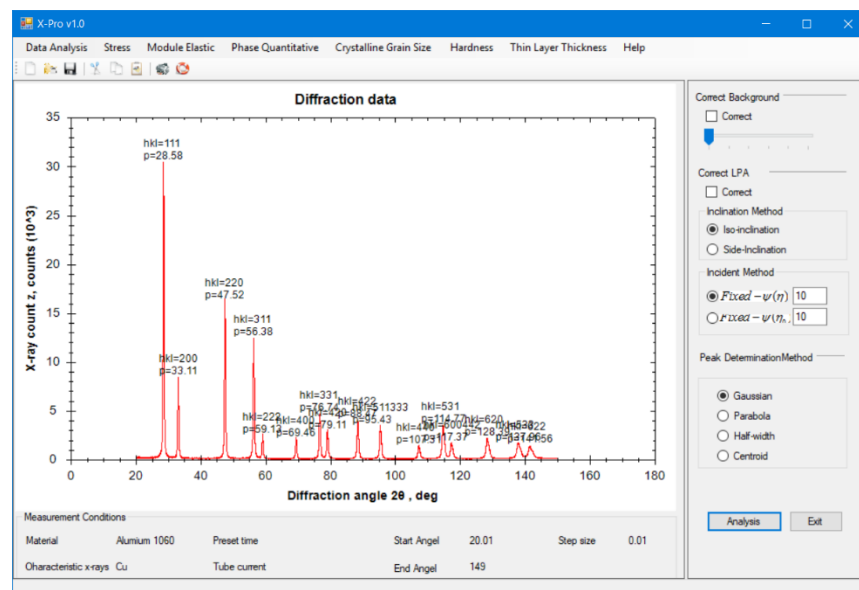


Figure 3. Main window for data analysis.

2.4. Smoothing

Figure 4 shows the diagram to smooth the roughly measured X-ray counts. The data are calculated from three data (x_1, y_1) , (x_i, y_i) , and (x_2, y_2) , with an interval of $n \times c$, where n is an integer and c is the step size of diffraction angle 2θ . The slope $\tan \alpha$ of the line (1,2) is:

$$\tan \alpha = \frac{y_2 - y_1}{x_2 - x_1} \tag{14}$$

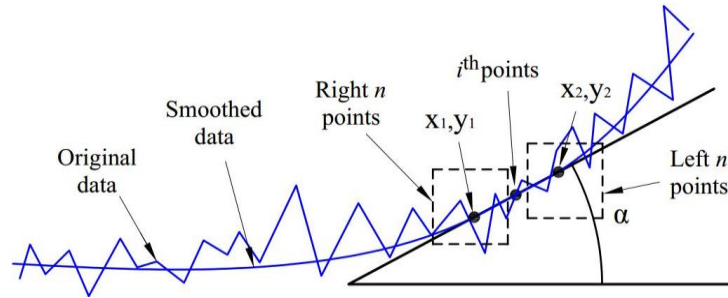


Figure 4. Determination of slope in smoothing technique.

For most normal measurements, the angle α is preset at 10° to distinguish between the diffraction peak and the background diffraction. The value of n can be preset between 1 and 10 to change the smoothing level.

2.5. Stress Measurement by X-ray Diffraction

Stress determination is based on lattice strain, which is expressed by the following Bragg’s law as:

$$n\lambda = 2d_{hkl} \sin\theta \tag{15}$$

where λ is wavelength, θ is Bragg angle, d_{hkl} is interplanar spacing, and n is an integer. If the Bragg angle θ in the stress direction is measured, the lattice spacing d_{hkl} , and thus the stress, is determined. Figure 5 shows the coordinate system 11, 22, and 33 on the surface of the specimen. The stress measurement direction L_3 is the normal plane of the crystalline matrix. The stresses σ_{ij} generate the strains ϵ_{ij} .

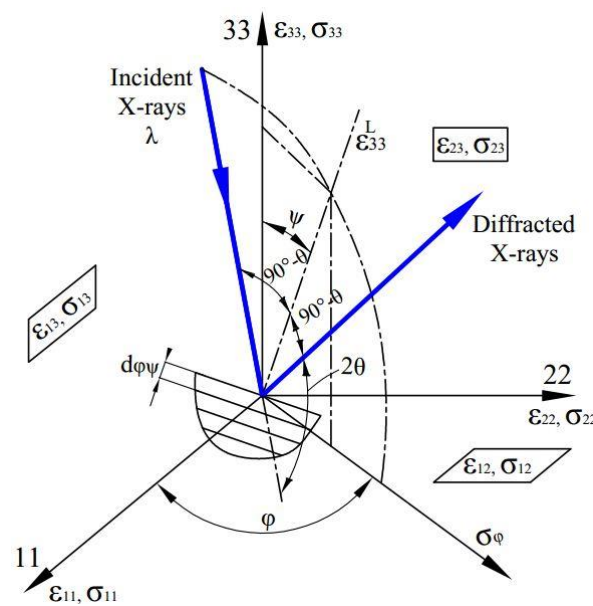


Figure 5. Relation between measured strain ϵ_{33}^L and the stresses σ_{ij} generated in the surface layer.

The strain ϵ_{33}^L in the measurement direction is determined from the lattice spacing d_{hkl} as [2,3]

$$\epsilon_{33}^L = \frac{d_{hkl} - d_0}{d_0} \tag{16}$$

where d_0 is the lattice spacing in the non-stress state. Equation (16) can be expressed in terms of strains ϵ_{ij} ($i, j = 1$ to 3) in the specimen coordinate system by the tensor transformation as

$$\epsilon_{33}^L = a_{3k}a_{3k}\epsilon_{3l} \tag{17}$$

where a_{3k}, a_{3l} are, respectively, the directional cosines between the normal of the diffraction plane and the axes 11, 22, and 33 to the direction cosine matrix as shown in Figure 5 by

$$a_{ik} = \begin{bmatrix} \cos \varphi \cos \psi & \sin \varphi \cos \psi & -\sin \psi \\ -\sin \varphi & \cos \varphi & 0 \\ \cos \varphi \sin \psi & \sin \varphi \sin \psi & \cos \psi \end{bmatrix} \tag{18}$$

From Equations (16)–(18), the relation between a strain in the laboratory system and the strain components in the specimen system is:

$$\begin{aligned} \epsilon_{33}^L = \frac{d_{hkl} - d_0}{d_0} = & \epsilon_{11} \cos^2 \varphi \sin^2 \psi + \epsilon_{12} \sin 2\varphi \sin^2 \psi + \epsilon_{22} \sin^2 \varphi \sin^2 \psi \\ & + \epsilon_{33} \cos^2 \psi + \epsilon_{13} \cos \varphi \sin 2\psi + \epsilon_{23} \sin \varphi \sin 2\psi \end{aligned} \tag{19}$$

From the elastic theory, strain–stress relation gives:

$$\begin{aligned} \epsilon_{33}^L = & \frac{1+\nu}{E} (\sigma_{11} \cos^2 \varphi + \sigma_{12} \sin 2\varphi + \sigma_{22} \sin^2 \varphi - \sigma_{33}) \sin^2 \psi \\ & + \frac{1+\nu}{E} \sigma_{33} - \frac{\nu}{E} (\sigma_{11} + \sigma_{22} + \sigma_{33}) \\ & + \frac{1+\nu}{E} (\sigma_{13} \cos \varphi + \sigma_{23} \sin \varphi) \sin 2\psi \end{aligned} \tag{20}$$

where E is the Young’s modulus and ν is Poisson’s ratio. For a plane stress state of the specimen, the third stress components are zero. Equation (20) becomes:

$$\epsilon_{33}^L = \frac{1+\nu}{E} \sigma_\varphi \sin^2 \psi - \frac{\nu}{E} (\sigma_{11} + \sigma_{22}) \tag{21}$$

where σ_φ is the term stress in the ϕ azimuth. Equation (21) can be written as:

$$d_{hkl} = d_0 \frac{1+\nu}{E} \sigma_\varphi \sin^2 \psi - d_0 \frac{\nu}{E} (\sigma_{11} + \sigma_{22}) + d_0 \tag{22}$$

If we put m as the slope of the straight line fitted to the lattice spacing d in the d_{hkl} - $\sin^2\psi$ diagram, the stress can be determined as:

$$\sigma_\varphi = \frac{m}{d_0} \left(\frac{E}{1+\nu} \right) \tag{23}$$

where m is the slope in Equation (22). Now, m is determined experimentally from the $\sin^2\psi$ diagram by fitting a straight line to a set of experimental points $(d_{hkl1}, \sin^2\psi_1), (d_{hkl2}, \sin^2\psi_2), \dots (d_{hkln}, \sin^2\psi_n)$ using the least-squared method. The precision coefficient (R^2) of the linear regression is determined as:

$$R^2 = 1 - \frac{SS_{residual}}{SS_{total}} = 1 - \frac{\sum_{i=1}^n (d_{hkli} - f_i)^2}{\sum_{i=1}^n (d_{hkli} - \bar{d}_{hkl})^2} \tag{24}$$

where $SS_{residual}$ and SS_{total} are the sum squared of regression error and sum squared total error of experimental values in comparison to the estimated values, f_i is predicted or estimated function, and $\bar{d}_{hkl} = \frac{1}{n} \sum_{i=1}^n d_{hkli}$ is the mean of the experimental data.

3. Results and Discussion

3.1. Analysis of Stress

The dialog box in Figure 6 allows us to select the material and its elastic constants used to determine stress. This also allows us to revise a material or add a new material and then save it to the program library. Figure 7 shows the display for choosing methods of peak position determination, and the correction factors used for stress computation. The corrected X-ray diffraction line, peak positions, and stress and their 95% confidential limits representing the reproducibility of the calculated value are shown.

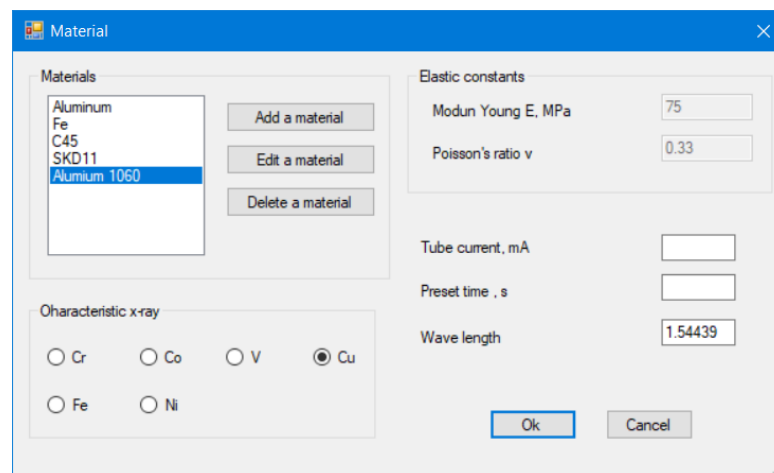


Figure 6. Elastic constants E and ν of common materials for stress computation.

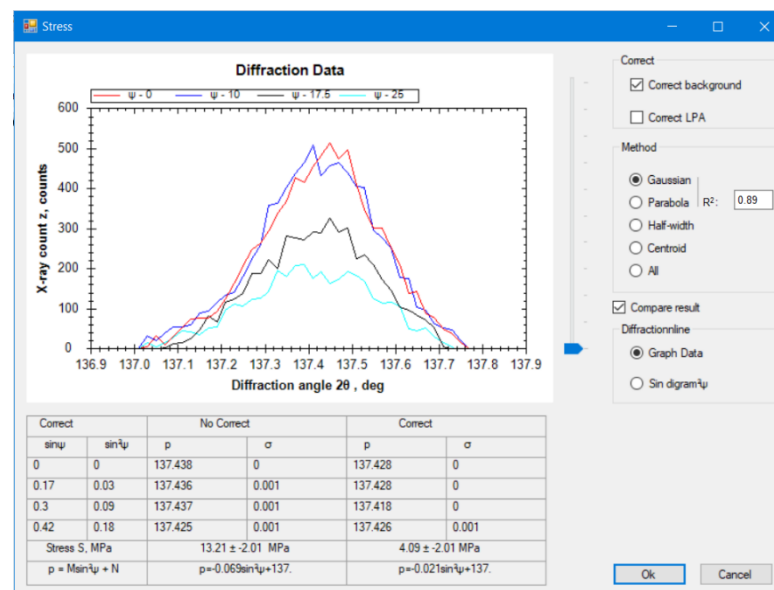


Figure 7. Peak positions and stress determination of aluminum alloy 1060.

The sample was made from aluminum alloy 1060 with dimensions of $250 \times 50 \times 5$ mm. The sample surface was ground to remove the surface layer of about 1 mm and then polished with emery paper to obtain the roughness of $0.64 \mu\text{m}$. Table 1 shows the experimental conditions for stress measurement using XRD.

Table 1. The experimental conditions for stress measurement using XRD.

Diffraction Method	Ω -Type, Fixed- η
Diffraction plane	(422) of hexagonal
Bragg angle	82.3°
Scanning range	132–142°
Step size	0.04°
Preset time	5 s
Voltage and current	20 kV and 10 mA

Table 2 shows the residual stresses of aluminum alloy 1060 calculated from XPro 2.0. The peak positions are computed using four methods of peak position determination Parabola, Gaussian, Half-width, and Centroid with their 95% confidence limits. They are also compared to the result computed from the commercial Origin. The stress values determined from the Parabola method and Gaussian curve method strongly agree with the Origin. They have a precision coefficient R^2 of fitting regression of 0.91 ± 0.06 and 0.89 ± 0.08 , respectively. In contrast, the Half-width and the Centroid methods gave much larger 95% confidential limits with lower R^2 of 0.72 ± 0.15 and 0.68 ± 0.18 , respectively. Therefore, the Parabola and Gaussian methods are the most suitable in XRD stress investigation.

Table 2. Residual stresses of alumina alloy 1060 (MPa).

Zones	XPert 2.0				Origin 3.0
	Gaussian	Parabola	Half-Width	Centroid	Gaussian
1	-17.3 ± 2.8	-17.3 ± 0.2	5.4 ± 19.7	7.5 ± 9.4	-25.3
2	-26.0 ± 8.9	26.0 ± 0.4	-3.2 ± 18.3	-2.4 ± 7.2	-30.4
3	13.2 ± 3.1	13.2 ± 0.4	11.6 ± 42.8	8.7 ± 8.5	10.1
4	-29.5 ± 6.0	-29.4 ± 0.6	-19.8 ± 27.7	-23 ± 9.6	-28.3

3.2. Analysis of Phase Compositions

The phase compositions of multi-phase materials (triple-phase carbide in this study) can be analyzed simply using XPro 2.0. Figure 8 is diffraction peaks in accordance with the diffraction planes for various phases. A formula for calculating the phase component was proposed in the previous studies [6,7] as the following.

$$q_x = \frac{\sum_{\alpha=1}^n E_{(hkl)_i^\alpha}^\alpha \lambda_j}{\sum E_{(hkl)_i^\alpha}^\alpha \lambda_j + \dots + \sum E_{(hkl)_i^n}^n \lambda_j} \quad (25)$$

Figure 9 represents the diffraction line from a three-phase material. The areas under a peak of a phase are the diffracted energy portion of that phase. Therefore, the phase composition is determined from the energy portion q_α , q_β , and q_γ diffracted from phases α , β , and γ with the total diffracted energy of material as:

$$\begin{aligned} q_\alpha &= \frac{\sum E_{(hkl)_i^\alpha}^\alpha \lambda_j}{\sum E_{(hkl)_i^\alpha}^\alpha \lambda_j + \sum E_{(hkl)_i^\gamma}^\gamma \lambda_j + \sum E_{(hkl)_i^\beta}^\beta \lambda_j} \\ q_\beta &= \frac{\sum E_{(hkl)_i^\beta}^\beta \lambda_j}{\sum E_{(hkl)_i^\alpha}^\alpha \lambda_j + \sum E_{(hkl)_i^\gamma}^\gamma \lambda_j + \sum E_{(hkl)_i^\beta}^\beta \lambda_j} \\ q_\gamma &= \frac{\sum E_{(hkl)_i^\gamma}^\gamma \lambda_j}{\sum E_{(hkl)_i^\alpha}^\alpha \lambda_j + \sum E_{(hkl)_i^\gamma}^\gamma \lambda_j + \sum E_{(hkl)_i^\beta}^\beta \lambda_j} \end{aligned} \quad (26)$$

where $E_{(hkl)_i}^\alpha \lambda_j$; $E_{(hkl)_i}^\beta \lambda_j$; $E_{(hkl)_i}^\gamma \lambda_j$ are the energy portion diffracted from phase α , β , γ from the i th plane $(hkl)_i$ for wavelength λ_j .

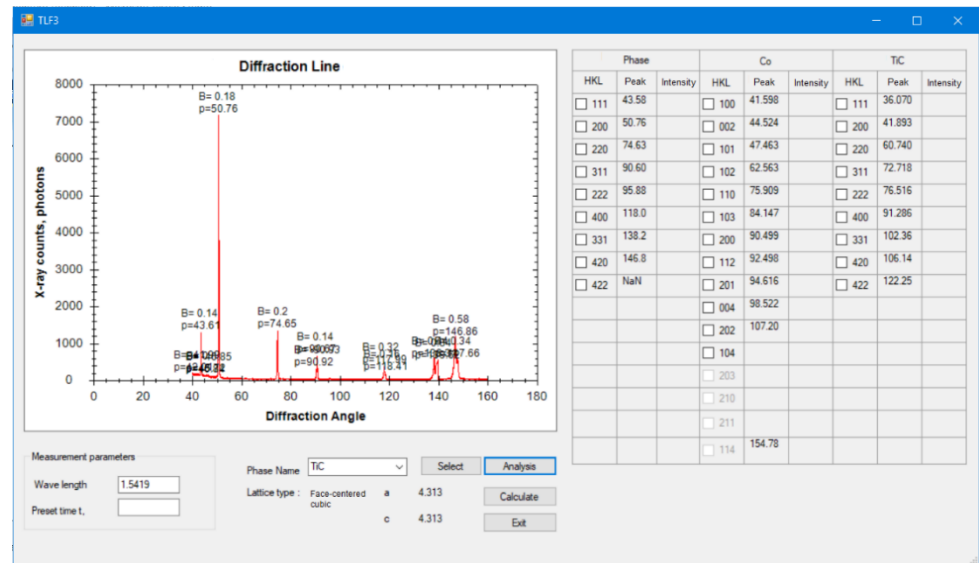


Figure 8. Dialog box for determining phase ratio of triple-phase carbide T15K6.

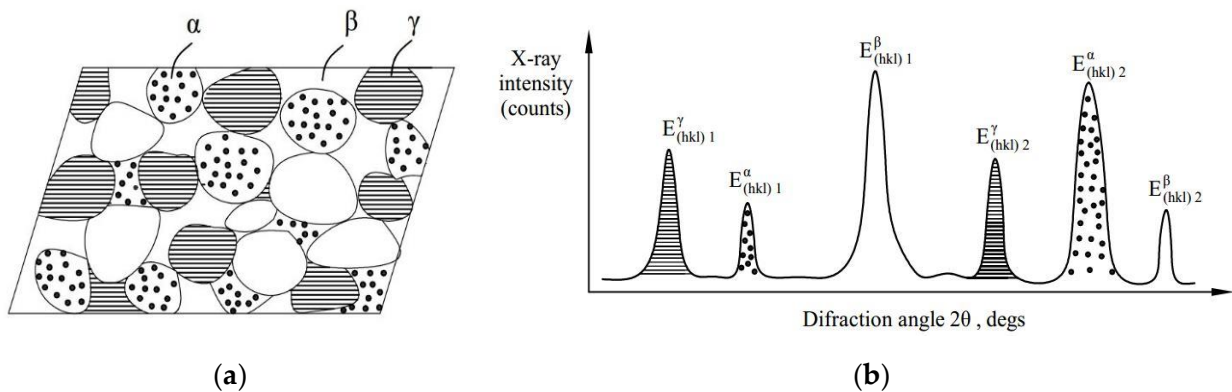


Figure 9. Microstructure of three-phase material (a,b) their peaks in a diffraction line.

Five samples of commercial triple-phase ceramic T15K6, containing three phases WC-TiC-Co, were prepared with dimensions of $15 \times 15 \times 20$ (mm). The average chemical compositions of the phases WC, TiC, and Co, respectively, were 78.63%, 14.17%, and 6.79%, together with their 95% confidence limits. Table 3 lists the XRD experimental conditions for analyzing phase compositions of carbide T15K6.

Table 3. XRD conditions for analyzing phase compositions of T15K6.

Measurement Method	Ω Type, Fixed- η
Preset time	5 s
Step size	0.02°
Voltage and current	20 kV and 10 mA

Table 4 compares the phase composition determined from the XRD method and chemical analysis method, which is known as a traditional and accurate technique for determining compositions. The results show good agreement between the methods, confirming the validity of proposed Equations (25) and (26) using the XRD technique.

Table 4. Phase compositions of carbide T15K6 (%).

Phase	XRD	Chemical Analysis
WC	77.86 ± 1.30	78.63 ± 0.59
TiC	14.96 ± 1.65	14.17 ± 0.52
Co	5.86 ± 1.47	6.79 ± 0.02

3.3. Evaluation of Hardness

Many studies have found that the full width of the maximum X-ray diffraction line (half-width) has a relation to the dislocation or disordering of crystalline matrixes. This is a result of many changes in the crystalline matrix in various industrial processes such as alloying by other metallic elements, hardening by quenching, plastic deformation, fatigue stress, etc. In this study, the hardening levels of quenched steel specimens were nondestructively investigated using XRD. A previous study has determined a linear relation between the Rockwell hardness HRC and the half-width of the diffraction line of quenched and tempered carbon steel [8]:

$$HRC = 87.85B + 20.34 \quad (27)$$

where $B = 2\sqrt{2 \ln 2} \sigma = 0.35\sigma$ is the half-width of the diffraction line and σ is the standard deviation of the Gaussian curve. In the case of the parabola method,

$$HRC = 103.01FHW + 21.31 \quad (28)$$

where FHW is the full width at half of the maximum X-ray intensity of the diffraction line.

Ten JIS-type S50C samples with dimensions of 50 × 50 × 200 mm were quenched at 850 °C in water, and then nine of them were tempered from 250 °C to 650 °C, in steps of 50 °C, for 45 min to eliminate the inhomogeneous distribution. The sample surfaces were polished with emery paper and then electrolytically polished to remove about 1 mm of the surface layer. The hardness of samples was measured using the Rockwell hardness testing method. Table 5 shows the experimental conditions for XRD measurement.

Table 5. XRD experimental conditions for JIS S50C steel.

Diffraction Type	Ω -Type, Fixed- η
Diffraction plane	(211)
Scanning range	80–85°
Step size	0.04°
Preset time	5 s
Voltage and current	20 kV and 10 mA

Figure 10 compares the HRC hardness with the line half-width. A straight line is fitted to the experimental points to establish the relation between FHW and HRC using Equations (27) and (28). From this practical linear relation, the hardness of quenched carbon steel can be easily estimated from the measured half-width. The same procedure can be applied to determine the hardness of quenched copper, stainless steel, plastically deformed steel, nickel alloys, etc.

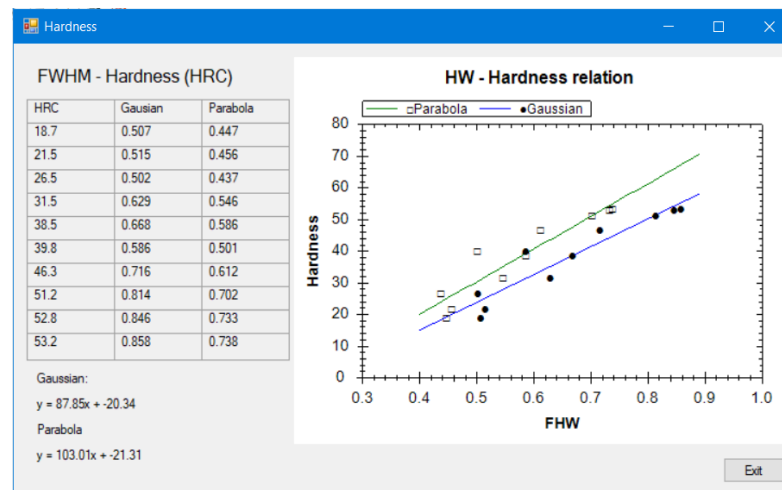


Figure 10. Dialog box for determining the hardness of quenched S50C.

3.4. Thickness of Coating Layer

To determine the thickness of the coating layer, the measurements using tilt angles ψ and ψ_0 were used. When “Count” is pressed, the thickness of the coating layer is determined, as shown in Figure 11. The coating thickness t is determined from the formulas as below [10]:

$$f(I, \psi, \psi_0, \theta) = \frac{I_\psi \cos \psi_0 [1 - \cot(\theta - \psi_0) \cot \theta]}{I_\psi \sin(\theta + \psi) [1 - \tan \psi \cot \theta]} \quad (29)$$

$$g(\mu, \psi_0, \theta) = \mu_f \left(\frac{1}{\cos \psi_0 [1 - \cot(\theta - \psi_0) \cot \theta]} - \frac{1}{\sin(\theta + \psi) [1 - \tan \psi \cot \theta]} \right) \quad (30)$$

$$t = \frac{\ln[f(I, \psi, \psi_0, \theta)]}{g(\mu, \psi_0, \theta)} \quad (31)$$

where θ is Bragg angle and μ and μ_f are the linear absorption coefficients of the substrate and coating layer used, respectively, and I_ψ is the maximum X-ray intensity in the fixed- ψ method.

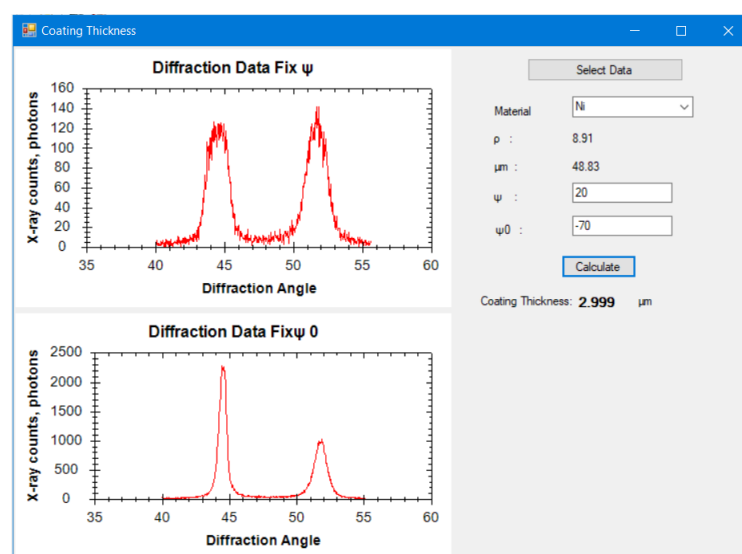


Figure 11. Dialog box for determining the thickness of the nickel-plating layer.

Three JIS-type SS400 samples with dimensions of $10 \times 40 \times 40$ mm were polished, electroplated for 6 to 30 min to obtain the thicknesses of $2 \mu\text{m}$, $2.25 \mu\text{m}$, $2.75 \mu\text{m}$, $3.25 \mu\text{m}$

and 3.5 μm , and observed directly under a microscope (MS). The thicknesses were measured by the Eddy current technique at nine positions in the central area of each sample to obtain the average values and their standard deviations.

Table 6 lists experimental conditions for XRD thickness measurements. Figure 11 shows the diffraction lines of the 3 μm plating sample. Table 7 compares the thickness of nickel-coating layers, measured using microscope techniques, Eddy current (EC), and XRD. The XRD technique allows determining 95% confidence limits of the computed values using a single measurement. The three techniques gave agreed thickness, and they are within the confidential limits.

Table 6. XRD conditions in thickness measurement of nickel-coating layer.

Diffraction Method	Ω -Type, Fixed- ψ and ψ_0
Scanning range	40–96°
Step size	0.03°
Preset time	2.5 s
X-ray characteristic	CuK α
Filter	Ni foil
Voltage and current	20 kV and 10 mA

Table 7. Thickness for nickel-plating layers with MS, ED, and XRD techniques (μm).

Samples	MS	EC	XRD
1	2.00	1.94 \pm 0.13	2.02 \pm 0.49
2	2.25	2.38 \pm 0.17	2.34 \pm 0.50
3	2.75	2.63 \pm 0.22	2.99 \pm 0.49
4	3.25	3.14 \pm 0.35	2.96 \pm 0.45
5	3.50	3.35 \pm 0.21	3.40 \pm 0.43

3.5. Determination of Crystalline Grain Size

The well-known Scherrer formula below is used to calculate a grain size t [1]:

$$t = \frac{K\lambda}{B \cos \theta_B} \quad (32)$$

where K is a constant referring to the cell geometry of lattice, where $K = 0.94$ for the cubic lattice; λ is X-ray wave length; B is the half-width of diffraction line; and θ_B is the Bragg angle of a peak position.

The experimental conditions for determining grain size of commercial synthetic zeolite ZSM-5 used in environment treatment are listed in Table 8. Table 9 represents the grain sizes of zeolite crystals, determined from XRD and observed using SEM techniques. It is shown that the XRD technique gives accurate results, in comparison to the SEM method.

Table 8. XRD conditions for thickness measurement of nickel-plating layer.

Diffraction Method	Ω -Type, Fixed- ψ
Scanning range	10–50°
Step size	0.03°
Preset time	3 s
Voltage and current	40 kV and 20 mA

Table 9. Grain size of zeolite crystals using XRD and SEM techniques (in μm).

Specimens	XRD	SEM
1	3.06 \pm 0.09	2.5
2	3.64 \pm 0.12	1 to 8

4. Conclusions

The following conclusions are made:

- a. Various functions for determining major mechanical properties of crystalline materials were integrated into the computational program as shown in Section 3;
- b. Generalized absorption functions for many measurement methods were embedded into the program to accurately determine the peak positions of the X-ray diffraction lines;
- c. The properties of many kinds of materials measured using XRD are compared to the conventional techniques, and they showed high agreement;
- d. The new computation program shows the high applicability of a universal X-ray diffraction device in evaluating crystalline materials.

Some proposals for further research include the evaluation of surface roughness or the measurement of various kinds of alloys and stainless steels.

Author Contributions: Conceptualization, V.P.N. and T.N.D.; Programming, V.P.N.; Data curation, A.V.H.N.; Specimen manufacturing, A.V.H.N.; Writing—Original draft preparation, V.P.N.; Writing—Review and editing, C.C.L. and T.N.D. All authors have read and agreed to the published version of the manuscript.

Funding: This research received no external funding.

Institutional Review Board Statement: Not applicable.

Informed Consent Statement: Not applicable.

Data Availability Statement: Data are included within the article.

Acknowledgments: The authors would like to express their appreciation to the staff of Ho Chi Minh City Center for Nuclear Techniques and the Metallurgy Laboratory at Ho Chi Minh City University of Technology and Education for their assistance.

Conflicts of Interest: The authors declare no conflict of interest.

References

1. Cullity, B.D. *Element of X-Ray Diffraction*, 3rd ed.; Prentice Hall: Upper Saddle River, NJ, USA, 2001; pp. 256–270.
2. Hauk, V. *Structural and Residual Stress Analysis by Nondestructive Method*, 1st ed.; Elsevier Science: Amsterdam, The Netherlands, 1997; pp. 136–168.
3. Noyan, I.C.; Cohen, J.B. *Residual Stress Measurement by Diffraction and Interpretation*; Springer-Verlag: New York, NY, USA, 1987.
4. Lu, J. *Handbook of Measurement of Residual Stress*; Society for Experimental Mechanics, The Fairmont Press Inc.: Atlanta, GA, USA, 1996; pp. 225–231.
5. Le, C.C.; Le, H.A. Structural analysis for nano-ceria using fourier analysis for X-ray diffraction line. In Proceedings of the 2012 International Conference on Green Technology and Sustainable Development, Ho Chi Minh City, Vietnam, 29 September 2012; HCMC-VNU Publishing House: Ho Chi Minh City, Vietnam, 2012.
6. Van, Q.H. Phase Determination of High Strength Ferrite-Austenitic Stainless Steel using X-Ray Diffraction. Master's Thesis, HCM City University of Technology and Education, Ho Chi Min, Vietnam, 2011. (In Vietnamese).
7. Cuong, L.C.; Son, N.H.; Nguyen, L.L.; Tuyen, L.A. Phase quantitative computation for multi-phase materials by means of X-ray diffraction. In Proceedings of the 4th International Conference on Green Technology and Sustainable Development, Ho Chi Minh City, Vietnam, 28 October 2016; HCMC-VNU Publishing House: Ho Chi Minh City, Vietnam, 2016.
8. Le, C.C. Determination of hardness of quenched and tempered steel using X-ray diffraction. *Vietnam J. Mech.* **2013**, *4*, 54–58.
9. Hind, A.R. *The Determination of Thin Film Thickness Using Reflectance Spectroscopy*; Agilent Technologies: Santa Clara, CA, USA, 2011; pp. 1–4.
10. Le, C.C.; Nguyen, T.T.; Luu, A.T. Determination of thickness of coating thin films using X-ray diffraction. *J. Sci. Technol.* **2015**, *105A*, 51–55.
11. Firrao, D.; Matteis, P.; Scavino, G.; Ubertalli, G.; Pozzi, C.; Ienco, M.G.; Piccardo, P.; Pinasco, M.R.; Costanza, G.; Montanari, R.; et al. Microstructural effects in face-centered-cubic alloys after small charge explosions. *Metall. Mater. Trans. A* **2007**, *38*, 2869–2884. [[CrossRef](#)]
12. Le, C.C. Development of Automated X-Ray Stress Measurement with Its Application. Ph.D. Thesis, Nagaoka University of Technology, Nagaoka, Japan, 2004.
13. Kurita, M.; Le, C.C.; Tatekawa, T. Development of a new automated X-ray stress analyzer. In Proceedings of the Second Japan-US Symposium on Advances in NDT, Kahuku, HI, USA, 21–25 June 1999; pp. 389–394.

14. Kurita, M. X-ray stress measurement by the Gaussian curve method. *Curr. Jpn. Mater. Res.* **1993**, *10*, 135–151.
15. Nguyen, V.P.; Le, C.C. Computation on generalized absorption function of thin film layer using x-ray analysis. In Proceedings of the 2nd International Conference on Green Technology and Sustainable Development, Ho Chi Minh City, Vietnam, 30 October 2014; HCMC-VNU Publishing House: Ho Chi Minh City, Vietnam, 2014.
16. Koistinen, D.P.; Marburger, R.E. A simplified procedure for calculating peak position in x-ray residual stress measurements of hardenel steel. *Trans. ASM* **1959**, *51*, 537–555.
17. Maedeh Sadat, Z.; Mohammad, H.S.; Mehdi, S. Effect of grinding parameters on the wear resistance and residual stress of HVOF-deposited WC-10Co-4Cr coating. *Surf. Coat. Technol.* **2016**, *307*, 886–891.
18. Luo, Q.; Jones, A.H. High-precision determination of residual stress of polycrystalline coatings using optimised XRD- $\sin^2\psi$ technique. *Surf. Coat. Technol.* **2010**, *205*, 1403–1408. [[CrossRef](#)]
19. Harish, N. *Structured Programming Approach*; TechMax Publications: Pune, India, 2013.
20. Brown, E. *Windows Forms Programming with C#*; Manning Publications Co.: Shelter Island, NY, USA, 2002.
21. Griffiths, I.; Adams, M.; Liberty, J. *Programming C# 4.0*; O'Reilly: Sebastopol, CA, USA, 2010.